



Full length article

Interface stability, mechanical and corrosion properties of AlCrMoNbZr/(AlCrMoNbZr)N high-entropy alloy multilayer coatings under helium ion irradiation



W. Zhang^{a,b}, M. Wang^c, L. Wang^d, C.H. Liu^e, H. Chang^d, J.J. Yang^{a,*}, J.L. Liao^a, Y.Y. Yang^a, N. Liu^a

^a Key Laboratory of Radiation Physics and Technology, Ministry of Education, Institute of Nuclear Science and Technology, Sichuan University, Chengdu 610064, PR China

^b Analytical and Testing Center, Sichuan University of Science and Engineering, Zigong 643000, PR China

^c Helmholtz-Zentrum Dresden-Rossendorf, Institute of Ion Beam Physics and Materials Research, Bautzner Landstr. 400, 01328 Dresden, Germany

^d Southwestern Institute of Physics, Chengdu 610225, PR China

^e College of Materials and Chemistry and Chemical Engineering, Chengdu University of Technology, Chengdu 610059, PR China

ARTICLE INFO

ABSTRACT

Keywords:

AlCrMoNbZr/(AlCrMoNbZr)N
Multilayer coating
High-entropy alloy
Ion irradiation
Interfaces
Nanoindentation
Electrochemical corrosion
Accident-tolerant fuel (ATF)

High entropy alloy (HEA) coatings are promising for use as accident-tolerant fuel cladding due to their outstanding high-temperature corrosion resistance. In this work, we investigated the interface stability, mechanical properties and corrosion resistance of AlCrMoNbZr/(AlCrMoNbZr)N multilayer coatings with individual layer thickness of 5 nm, 10 nm and 50 nm, subjected to helium (He) ion irradiations: 400 keV He⁺ ions with fluences of 8×10^{15} ion/cm² and 8×10^{16} ion/cm². We determined that He bubbles are not observed in any of the multilayer coatings after a helium ion irradiation process with 400 keV He ions and a fluence as high as 8×10^{16} ion/cm². Although intermixing and chemical reaction in the peak damage region of the AlCrMoNbZr/(AlCrMoNbZr)N multilayer coating with 5 nm monolayer thickness are induced by the high fluence He ion irradiation, the FCC structure remained, and no intermetallic compounds are detected. Moreover, we found that the AlCrMoNbZr/(AlCrMoNbZr)N multilayer coating with the monolayer thickness of 50 nm has better interface stability during the irradiation process. Nanoindentation tests reveal that the hardness of all multilayer coatings decreased for low and high fluences, which is mainly due to the thermal effect caused by irradiation. In addition, the electrochemical corrosion test show that AlCrMoNbZr/(AlCrMoNbZr)N multilayer coating 50 nm coatings has better corrosion resistance than AlCrMoNbZr/(AlCrMoNbZr)N multilayer coating 5 nm coatings under high fluence He irradiation. The corrosion resistance of the multilayer coating depends on the stability of the multilayer interface. Our results show that the AlCrMoNbZr/(AlCrMoNbZr)N multilayer coating with a monolayer thickness of 50 nm had better interface stability, mechanical properties and corrosion resistance than the AlCrMoNbZr/(AlCrMoNbZr)N multilayer coating with a per layer thickness of 5 nm under high fluence He irradiation. This work reveals that high-entropy alloy multilayer coatings could have potential applications as an accident-tolerant fuel cladding coating in light water reactors.

1. Introduction

Developing a protective coating for the surface of existing Zr alloy cladded equipment is one of the most important accident-tolerant fuel approaches. Such a protective coating should be able to improve the high-temperature steam corrosion resistance effectively and reduce the hydrogen generation rate of the zirconium alloy cladding during beyond design basis (BDB) accident scenarios (e.g., a loss-of-coolant accident (LOCA)) [1]. In recent decades, several types of coating materials have been investigated, such as MAX phase materials (Ti₂AlC, Cr₂AlC)

[2,3], metallic-like coatings (Cr, FeCrAl) [4,5] and multilayer coatings (TiN/TiAlN, Cr/CrAl) [6,7]. These coating materials exhibit outstanding corrosion resistance in high-temperature water or steam environments. High-entropy alloy (HEA) has been proposed as a new term which can also serve as a protective coating to enhance the high-temperature water corrosion resistance for Zr alloy cladding [8,9]. HEAs are composed of at least five principal elements with atomic content between 5 and 35 at.% that form random solid solutions with a simple FCC/BCC crystal lattice structure instead of commonly complex intermetallic compounds [10]. The complex compounds construct an

* Corresponding author.

E-mail address: jjyang@scu.edu.cn (J.J. Yang).

environment with specific properties, e.g., the complicated random-arranging of alloying elements, the atomic-scale local chemical environment and the short-range three-dimensional mode of cluster motion. A lot of extraordinary properties are thus induced, such as high thermal stability [11,12], good high-temperature strength and hardness [13,14], excellent corrosion resistance [15] and outstanding irradiation resistance [16,17]. Then, HEA coatings were also developed that exhibited good corrosion resistance [8,9] and radiation resistance [18–20].

However, the surface coating of Zr alloys is also subjected to intense irradiation inside nuclear reactors or during accident conditions, where the corresponding displacement damage with subsequent formation of defects in the coating materials can be generated. This results in structural disorder, swelling, radiation hardening and reduction of the service ability of the coating material. Thus, the irradiation effect on the coatings could not be neglected. Unfortunately, few studies have focused on the radiation resistance of protective coatings [21–23]. As previously established, the grain boundaries (GBs) of the coating and the heterointerface are capable of absorbing radiation-induced defects and blocking the migration of dislocations to improve the radiation resistance of the coating material [24,25]. Based on this concept, multilayer coatings with high interfacial density distribution exhibit better radiation tolerance and stability of the coating structure and mechanical properties than conventional single-layer coatings [26]. The promising multilayers include metallic multilayers (Cu/Nb, Cu/W, Cu/V, Fe/W, Al/Nb and V/Ag) [27–32], ceramic multilayers (AlN/TiN and TiN/MgO) [33,34] and composite layers of metal or alloy and ceramic (Al/B₄C and FeCr/TiO₂) [35,36]. The multilayer coating structure with the design of multiple interfaces is an effective way to enhance the radiation resistance of the coating.

In our previous work, we reported that AlCrMoNbZr/(AlCrMoNbZr)N multilayer coatings with equal individual layer thicknesses (5 nm, 10 nm and 50 nm) have a good high-temperature corrosion performance [8] that can effectively improve the high-temperature corrosion performance of Zr alloys. An AlCrMoNbZr/(AlCrMoNbZr)N multilayer coating as a cladding protective coating in the nuclear reactor would be subject to long-term irradiation. Although several studies have shown that high-entropy alloys have excellent irradiation damage resistance [16,17], it is crucial to investigate the stability of the microstructures, mechanical and corrosion resistance of coatings after irradiation. In addition, there is a lack of research data on the irradiation of high-entropy alloy coatings and their multilayer coatings, especially the effect of irradiation on their corrosion and mechanical corrosion properties. This work mainly focuses on the effects of 400 keV helium irradiation with different fluences on the interfacial structure, hardness and corrosion resistance of AlCrMoNbZr/(AlCrMoNbZr)N multilayer coatings.

2. Experimental

AlCrMoNbZr/(AlCrMoNbZr)N multilayer coatings with equal thickness AlCrMoNbZr and (AlCrMoNbZr)N monolayers were deposited on Si (100) substrates by magnetron co-sputtering technique, and the thickness of individual layer was 5, 10 and 50 nm, respectively. Correspondingly, the deposition time of (AlCrMoNbZr)N monolayers is 24 s, 48 s, 240 s. The total coating thickness is approximately 2 μm. Details regarding the deposition process can be found elsewhere [8]. Considering that zirconium alloy cladding is located in the central region of a light water reactor, the typical displacement damage is approximately 2–3 displacement per atom (dpa) per year. The displacement damage rate has a negative relationship with distance from the core due to neutron moderation as energy loss through collisions with the coolant and core materials [37]. Therefore, the corresponding fluence of the He ion (SRIM simulation) with displacement damage up to 2–3 dpa was used to simulate the material radiation damage by neutron irradiation. Radiation experiments were carried out at room

temperature (~25 °C) using a He ion beam with an irradiation energy of 400 keV and the two fluences of 8×10^{15} and 8×10^{16} ions/cm² by accelerator at the Ion Beam Center of the Helmholtz-Zentrum Dresden Rossendorf. The beam current is around 20 microamps. The temperature increase from beam heating was estimated to be lower than 300 °C. The Stopping and Range of Ions in Matter (SRIM) program in the Monolayer Collision Steps model [38] was used to calculate the depth profiles of dpa and He concentration. The dpa was calculated using the following formula: $dpa = N_d N_i / N_a$ (N_d is the primary displacement unit length, N_a is the atomic density of the target and N_i is the irradiation fluence) [38]. In addition, to distinguish the effect of irradiation from that of heat treatment, the 5 nm AlCrMoNbZr/5 nm (AlCrMoNbZr)N multilayer coating (named as AlCrMoNbZr/(AlCrMoNbZr)N 5 nm) was annealed at the same time and temperature as the irradiated material.

To investigate the phase structure of the coating after irradiation, X-ray diffraction (XRD, D2 PHASER, AXS Bruker) measurements were carried out in the Bragg–Brentano θ–θ geometry and Cu K_α radiation with a wavelength of 0.154184 nm. The samples were scanned from 10° to 90° with a resolution of 0.01° per step and a step time of 0.5 s. The microstructure of the as-deposited and irradiated multilayer coating was analyzed by spherical aberration-corrected transmission electron microscopy equipped with two aberration correctors (ACTEM, FEI Titan Themis 80–300). The local element distribution (maps and line scans) of the multilayer coating was analyzed by highly efficient (4 quadrant) energy dispersive X-ray (EDX) spectroscopy at 300 kV with a point-to-point resolution of 0.2 nm and a maximum resolution of 0.06 nm in a high-angle annular dark field (HAADF) high-resolution scanning transmission electron microscopy (STEM). The samples for cross-sectional transmission electron microscopy (TEM) were prepared by an FEI HELIOS NanoLab 600i Focused Ion Beam (FIB) system.

A nanoindenter (NHT2, Anton Paar) was used to measure the nanohardness of the coating. The indentation depth was ensured to be less than 1/10 of the coating thickness to avoid the substrate effect. To effectively compare the corrosion performance of the coatings after irradiation, an electrochemical corrosion method was carried out on a three-electrode electrochemical system (CHI600E, CH Instruments Inc. USA) at room temperature (25 °C). The specimen was immersed in 3.5% sodium chloride solution for 30 min before collecting the potentiodynamic polarization data to reach a quasi-stationary value for the open circuit potential (OCP). The OCP-dependent polarization of the coatings was tested from an initial potential of 0.25 V to a final potential of 0.3 V at a scan rate of 0.5 mV/s.

3. Results and discussion

3.1. Microstructure of as-deposited multilayer coating

Cross-sectional TEM images of as-deposited AlCrMoNbZr/(AlCrMoNbZr)N 5 nm and AlCrMoNbZr/(AlCrMoNbZr)N 50 nm multilayer coatings are shown in Fig. 1(a) and (b), respectively. The sharp interfaces between the AlCrMoNbZr and (AlCrMoNbZr)N layers can be observed. The microstructure of the AlCrMoNbZr/(AlCrMoNbZr)N 10 nm multilayer coatings was reported in ref. [8]. The inserted selected area electron diffraction (SAED) patterns indicate that both multilayer coatings are FCC structures with (111), (200), and (220) planes. To further confirm the microstructure, high-resolution TEM (HRTEM) was carried out and is shown in Fig. 1(c) and (d). The (AlCrMoNbZr)N layer illustrates an FCC structure, whereas the AlCrMoNbZr layer is amorphous, indicating that the multilayer coating is a mixture of amorphous and FCC-structured coatings. Meanwhile, it can be observed that the amorphous layer appeared in the (AlCrMoNbZr)N layer of the FCC structure in the 5 nm and 50 nm coatings. The reason is assumed to be the suppressed grain growth by the high cooling rate of the non-thermodynamic equilibrium magnetron sputtering method [39]. The atomic size polydispersity, mixing enthalpy ΔH_{mix} , and

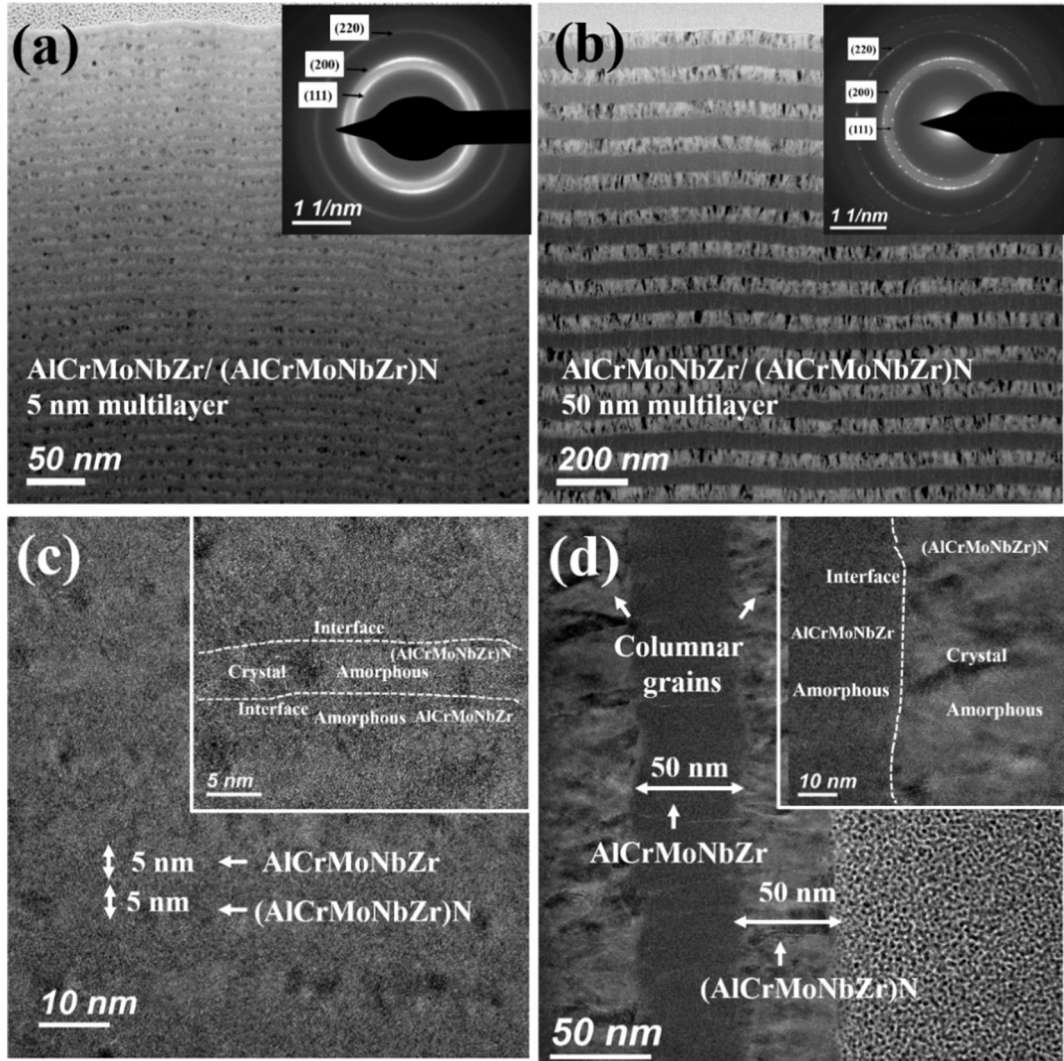


Fig. 1. (a) Cross-sectional TEM image of as-deposited AlCrMoNbZr/(AlCrMoNbZr)N 5 nm multilayer coating; (b) Cross-sectional TEM image of as-deposited AlCrMoNbZr/(AlCrMoNbZr)N 50 nm multilayer coating; (c) Magnification cross-sectional TEM image and HRTEM image of as-deposited AlCrMoNbZr/(AlCrMoNbZr)N 5 nm multilayer coating; (d) Magnification cross-sectional TEM image and HRTEM image of as-deposited AlCrMoNbZr/(AlCrMoNbZr)N 50 nm multilayer coating.

mixing entropy ΔS_{mix} may also considerably affect the structure of the HEA coatings [40]. In addition, the growth of columnar crystals evolved with the thickness of a single layer. When the thickness of the monolayer was 50 nm, the (AlCrMoNbZr)N layer consists of columnar crystals, and the columnar crystal size is approximately 30 nm; however, no columnar crystals appear for the 5 nm monolayer thickness. Increasing the thickness of a single layer requires a longer deposition time. The substrate temperature rises rapidly during the deposition process and has a heat dissipation direction perpendicular to the substrate, which promotes the formation and growth of columnar crystals.

Furthermore, EDS elemental mapping and line scans were carried out to measure the typical chemical compositions of Al, Cr, Mo, Nb, Zr and N, as shown in Fig. 2(a) and (b). The EDS mapping illustrates the relative distribution of all elements. The light color area shown in Fig. 2(a) and (b) indicates a high concentration of a given element, while in dark color area the concentration is low. The N has a distinct layered distribution with a high N content in the (AlCrMoNbZr)N layer and almost no N in the AlCrMoNbZr layer. The five elements of Al, Cr, Mo, Nb and Zr also had a layered distribution, and the content of elements in the AlCrMoNbZr layer was higher than that in the (AlCrMoNbZr)N layer. Meanwhile, the EDS line scan spectra show that the six elements of Al, Cr, Mo, Nb, Zr and N in both multilayer coatings

exhibit periodic changes in good agreement with our deposition process [8].

3.2. Microstructural evolution of irradiated multilayer coating

Fig. 3 shows the SRIM simulated damage profiles in the AlCrMoNbZr/(AlCrMoNbZr)N 50 nm multilayer coating after 400 keV helium (He) ion irradiation with an irradiation fluence of 8×10^{16} ion/cm². One major disadvantage of a layered morphology is that the simulation of the AlCrMoNbZr/(AlCrMoNbZr)N 5 nm multilayer coating did not provide a complete depth-dependent spectrum due to the limitation of the SRIM program. The AlCrMoNbZr/(AlCrMoNbZr)N 5 nm and 50 nm multilayer coating can be equivalent to the same component of the Al_{0.14}Cr_{0.15}Mo_{0.16}Nb_{0.15}Zr_{0.14}N_{0.26} compound. Hence, the depth profile of He was similar in both multilayer coatings. As the simulation in Fig. 3, in AlCrMoNbZr/(AlCrMoNbZr)N 50 nm, the He concentration showed a Gaussian distribution with a peak value of ~4 at.% at a depth of ~1100 nm. The peak damage induced by He collisions in the coating is approximately 2.7 dpa at 1100 nm, and the radiation damage extends to a maximum depth of ~1350 nm upon He ion irradiation at 400 keV.

XRD tests were performed to investigate the microstructure of all multilayer coatings after irradiation with fluences of 8×10^{15} and

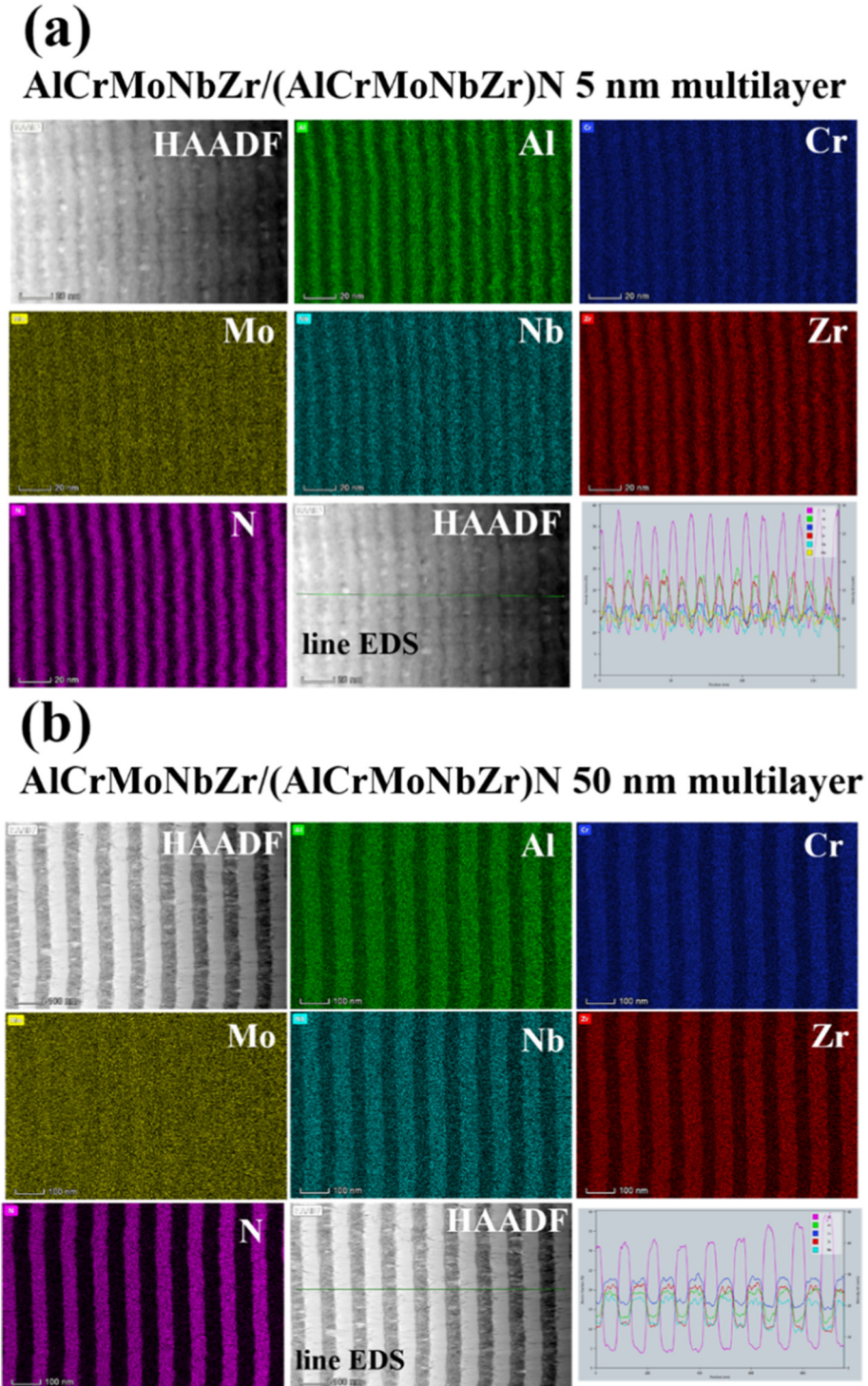


Fig. 2. EDS mapping and EDS line scan of as-deposited AlCrMoNbZr/(AlCrMoNbZr)N multilayer coating: (a) AlCrMoNbZr/(AlCrMoNbZr)N 50 nm multilayer coating; (b) AlCrMoNbZr/(AlCrMoNbZr)N 5 nm multilayer coating.

8×10^{16} ion/cm², and the results are shown in Fig. 4. Combined with the TEM data of the as-deposited coating (Fig. 1), the (AlCrMoNbZr)N layer in all multilayer coatings exhibit an FCC structure with a (111) plane preferred orientation. In most cases, after ion irradiation, the AlCrMoNbZr/(AlCrMoNbZr)N multilayer coating has a stable FCC structure without an intermetallic phase. Moreover, the peak intensity of the (111) plane significantly decreased and was accompanied by a slight shift to higher angles. The (200) orientation was preferred for growth, and the FWHM of the diffraction peaks of the (200) plane is

obviously broadened, indicating the grain refinement of the coating after irradiation. Kinetic constraints are assumed to affect the preferential orientation, as proposed by Petrov, Ensinger, and Hultman et al. [41–43]. The change in the grain growth orientation depends on the ion beam direction. On the other hand, the (111) plane of the NaCl structure is more densely packed than the (100) plane, and the second and third planes of the latter are more open to ions. Consequently, the (200) planes have higher probabilities of survival than the (111) planes under ion bombardment because of anisotropic collision cascades.

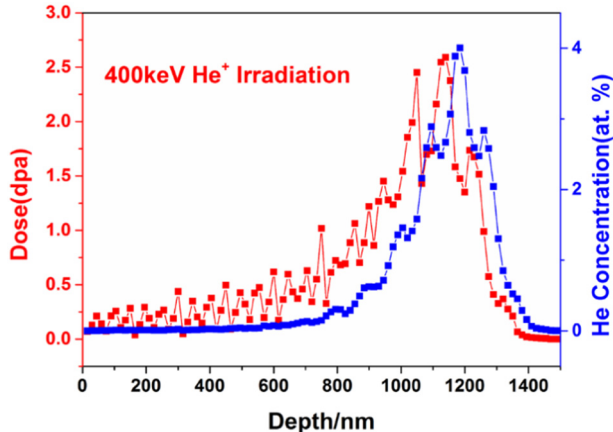


Fig. 3. SRIM calculation of damage and He concentration profile in AlCrMoNbZr/(AlCrMoNbZr)N 50 nm multilayer coating with a fluence of 8×10^{16} ion/cm 2 under 400 keV He ion irradiation.

TEM experiments were performed to study the microstructure of irradiated samples in detail. Fig. 5 shows a cross-sectional TEM micrograph of the AlCrMoNbZr/(AlCrMoNbZr)N 5 nm multilayer coating irradiated by He ions with a fluence of 8×10^{16} ion/cm 2 . In the region with the highest He concentration according to the SRIM simulation (Fig. 3), no detectable He bubbles were observed in both of the bright- and dark-field cross-section TEM images, as shown in Fig. 5(a) and (b). At similar irradiation fluences, large helium bubbles were clearly observed at the monolayer and multilayer interfaces in Cu/Nb [27], Cu/V [29], Fe/W [30] and V/Ag [32] multilayer systems. Comparison of these data shows that the AlCrMoNbZr/(AlCrMoNbZr)N multilayer coating can effectively inhibit the growth of helium bubbles. He irradiation can produce a large number of vacancies in the coating, which will lead to a decrease in the interplanar spacing of the coating. The results are consistent with the XRD diffraction peak shifting to a high angle after irradiation [28]. Moreover, the vacancies easily form helium-vacancy complexes with He. The slow diffusion effect of the high-entropy alloy makes a higher migration energy barrier for the helium-vacancy complex, which can effectively prevent the aggregation of the helium-vacancy complex and further inhibit the growth of the helium bubble. Meanwhile, a large quantity of multilayer interfaces plays the role of sink positions, where the point defects migrate and annihilate instead of forming relatively stable aggregates (voids, clusters and helium bubbles) [32]. In addition, the concentration of helium introduced by irradiation has a significant effect on the growth of helium bubbles. It is difficult to form observable helium bubbles at low helium concentrations [44]. Therefore, the AlCrMoNbZr/(AlCrMoNbZr)N multilayer coating exhibits good performance in suppressing the growth of the He bubbles. In addition, the amorphous region in the (AlCrMoNbZr)N layer of the FCC structure is larger than that in the as-deposited (AlCrMoNbZr)N layer after irradiation, as demonstrated in Fig. 5(c). This TEM result is in good agreement with the XRD data after irradiation. The thermal spike brought about by the ion beam was quite strong according to the small volume of the irradiated layer; therefore, the alloy will be partially melted and then cool rapidly through thermal conduction to the surroundings. HEAs have strong atomic-scale stresses because of the different sizes of the constituent elements, which promotes the formation of amorphous elements after irradiation.

The cross-section TEM images of the irradiated AlCrMoNbZr/(AlCrMoNbZr)N 5 nm multilayer coating interface structures in different irradiated regions are shown in Fig. 6. It can be observed that the multilayer coating has a distinct multilayer interface in the near-surface region, and the inserted selected area electron diffraction shows that the coating in this region has an FCC structure (Fig. 6(b)). The corresponding EDS mapping data also show that the five elements of Al, Cr,

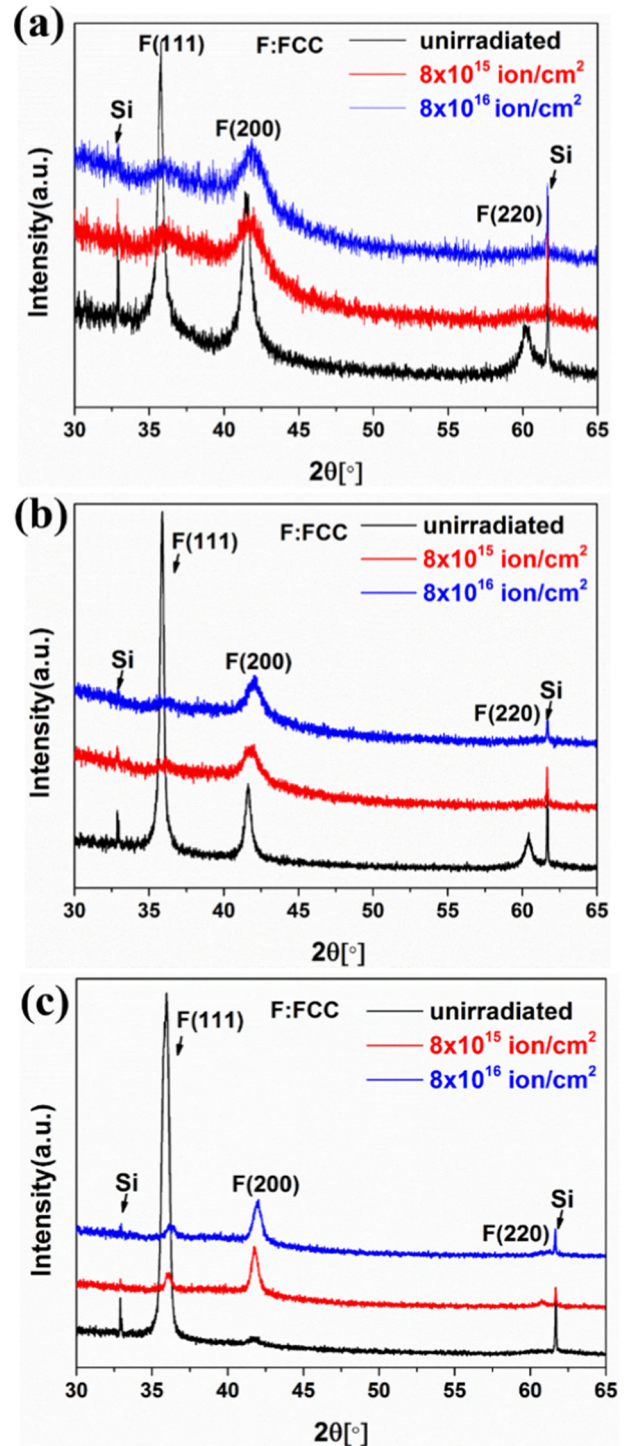


Fig. 4. Evolution of XRD patterns of the (a) AlCrMoNbZr/(AlCrMoNbZr)N 5 nm multilayer coating, (b) AlCrMoNbZr/(AlCrMoNbZr)N 10 nm multilayer coating and (c) AlCrMoNbZr/(AlCrMoNbZr)N 50 nm multilayer coating.

Nb, Zr and N have clearly layered distributions, as shown in Fig. 7(a). However, the multilayer coating shows the disappearance of interfaces in the peak damage region. The EDS mapping data indicates that the six elements of Al, Cr, Mo, Nb, Zr and N in the AlCrMoNbZr and (AlCrMoNbZr)N layers clearly diffused. The further quantitative EDS line scan results indicate that the six elements of Al, Cr, Mo, Nb, Zr and N are uniformly mixed and distributed, and the corresponding atomic fractions are 16 at.%, 21 at.%, 16 at.%, 13 at.%, 21 at.% and 13 at.%, respectively. Although the multilayer interface disappears and the

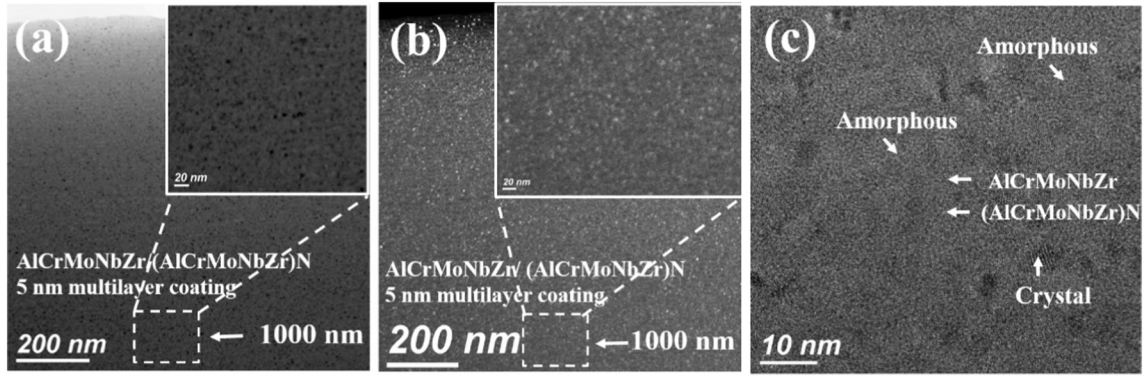


Fig. 5. TEM cross-sectional images of an AlCrMoNbZr/(AlCrMoNbZr)N 5 nm multilayer coating after He irradiation with a fluence of 8×10^{16} ion/cm²: (a) bright field, (b) dark field and (c) cross-sectional HRTEM image in the region of 1000 nm underneath the coating surface.

nitrogen content is 13 at.%, selective electron diffraction shows that the peak damage region still maintained the FCC structure, and no intermetallic compounds were detected since the high-entropy nitride alloy had an FCC structure for a wide range of nitrogen content [45]. A closer look at the peak damage region in the coating was studied by high-resolution TEM and is shown in Fig. 6(d). Fast Fourier Transform (FFT) diffraction was taken from the areas indicated by arrows in the figure. Part of the amorphous (AlCrMoNbZr)N layer combines with the AlCrMoNbZr amorphous layer to form a large amorphous region across the

whole (AlCrMoNbZr)N layer thickness.

Interface mixing in multilayer coatings occurs due to collision cascades [46] and thermal spikes around the ion tracks during He ion irradiation [47], both of which are strongly controlled by chemical driving forces. Here, the affected region can be divided into two parts: the collision cascade regime and the thermalizing regime. The time needed to rest all atoms in the collision cascade regime after a single ion irradiation is $\sim 10^{-13}$ s, while the corresponding time for equalizing the local temperature with the neighboring surroundings in the

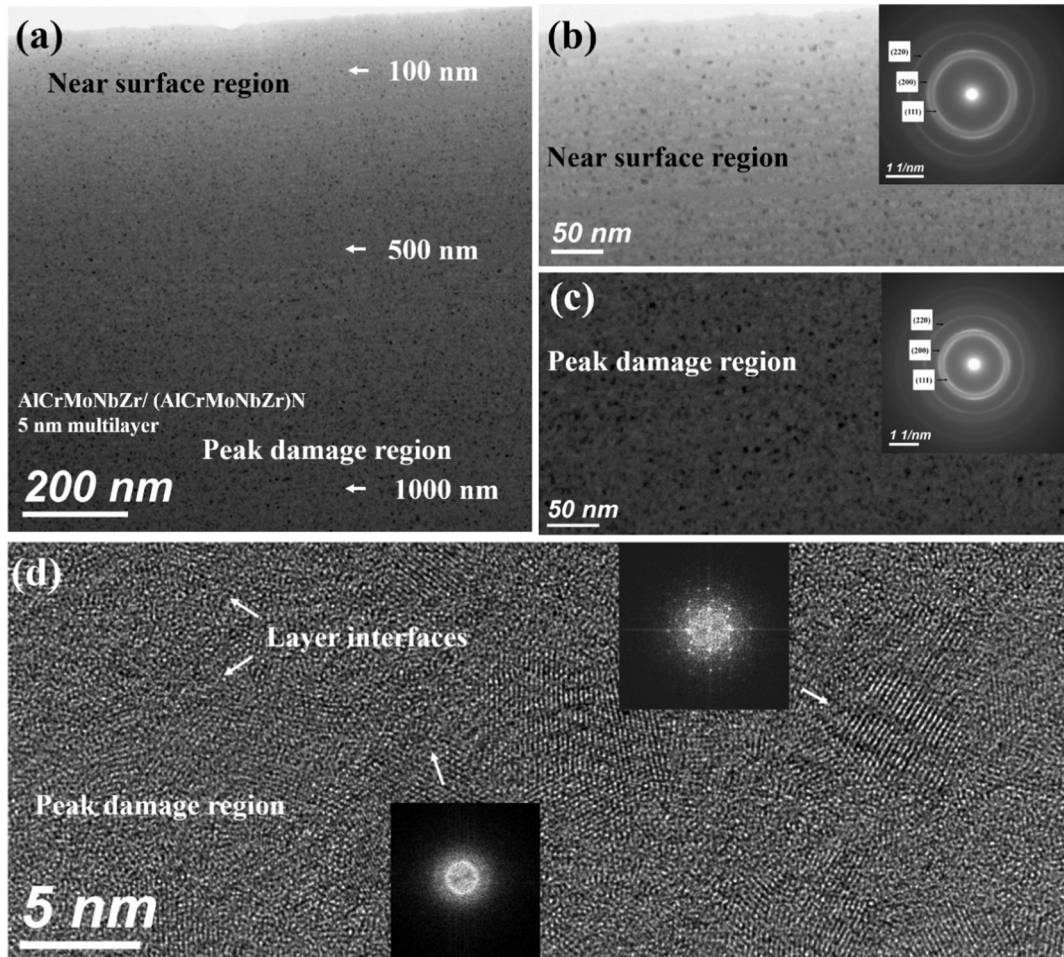


Fig. 6. (a) Cross-section TEM image of the AlCrMoNbZr/(AlCrMoNbZr)N 5 nm multilayer after He irradiation with a fluence of 8×10^{16} ion/cm²; (b) cross-section TEM image in the near surface region and peak damage region; (c) cross-section HRTEM image in the peak damage region of 1000 nm underneath the coating surface.

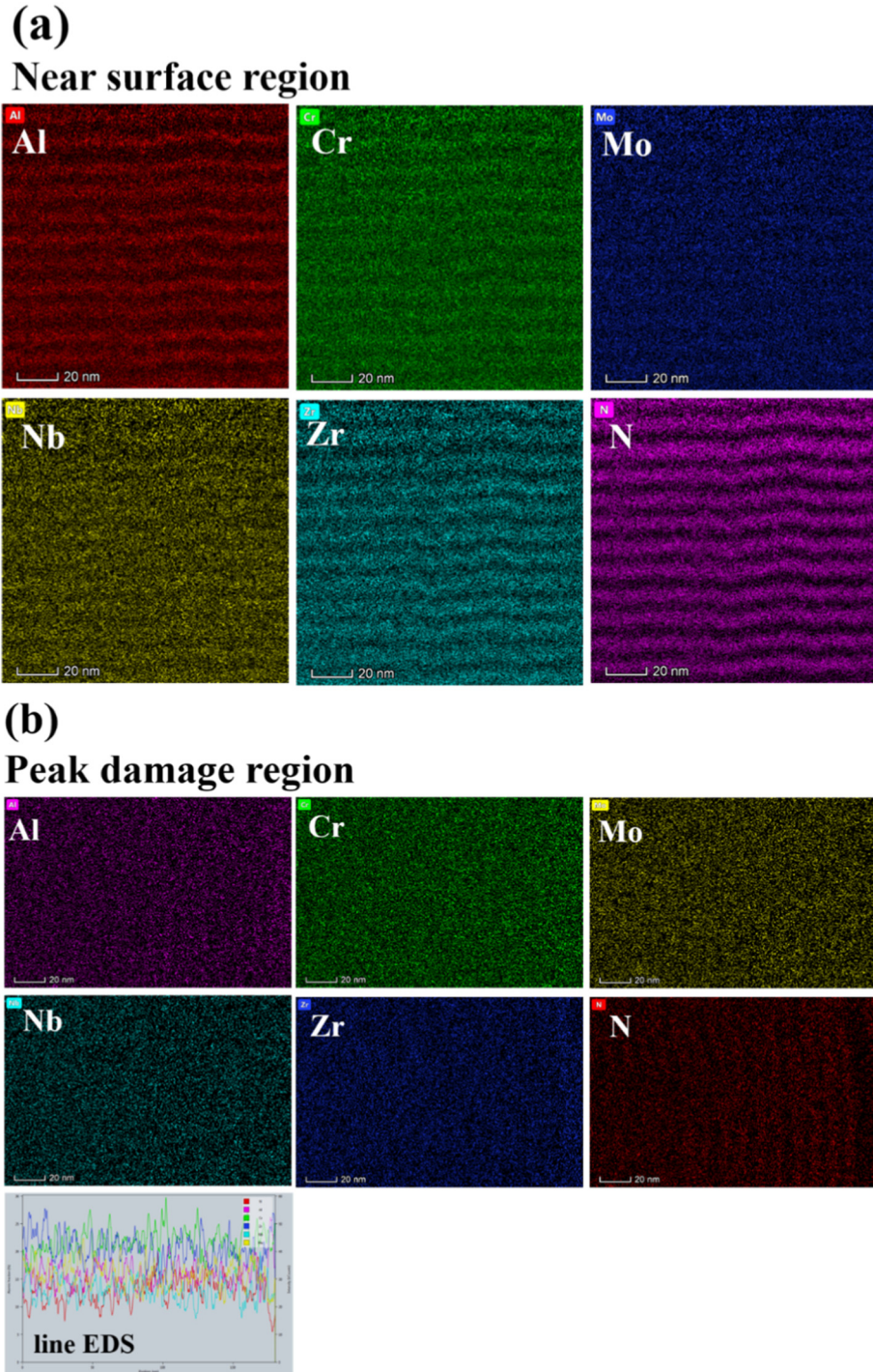


Fig. 7. EDS mapping and EDS line scan of the AlCrMoNbZr/(AlCrMoNbZr)N 5 nm multilayer coating after He irradiation with a fluence of 8×10^{16} ion/cm²: (a) EDS mapping in the near surface region; (b) EDS mapping and EDS line scan in the peak damage region.

thermalizing regime in a thermal spike is much longer, approximately 10^{-10} – 10^{-9} s [47,48]. The thermalizing regime is where the chemical driving forces play its role. If the components are miscible or chemically reactive, the initial ballistic mixing is strengthened; if not, the components remain unmixed due to the occurrence of dynamic demixing. Moreover, for multilayer coating systems which are miscible or chemically reactive, or a multilayer coating with thinner monolayer thickness, the rapid collision cascade regime induces a thorough intermixing of components. In this case the chemical forces driving demixing are effective. With a monolayer thickness, the collision cascade mixing is much weaker and can be compensated by dynamic demixing,

so the layers remain unmixed.

In the AlCrMoNbZr/(AlCrMoNbZr)N 5 nm multilayer coating, the AlCrMoNbZr and (AlCrMoNbZr)N layers have the same five elements of Al, Cr, Mo, Nb and Zr with different concentrations, while the N element has a great concentration difference. Therefore, under thermal shock, the five elements of Al, Cr, Mo, Nb and Zr easily interdiffused and reacted easily with N to form the corresponding nitride, leading to the formation of a nitride with an FCC structure. In addition, the extremely short-time high-temperature thermal shock is a non-thermal equilibrium process, making it easy for these elements with different atomic radii to form an amorphous layer.

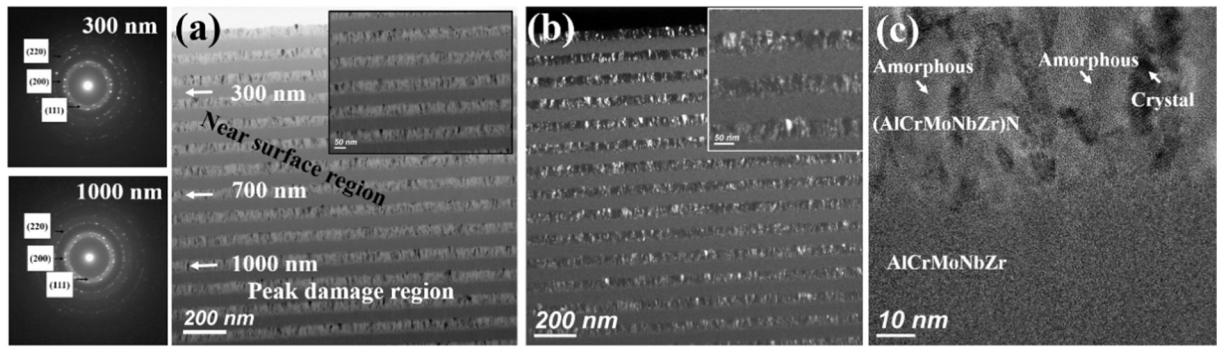


Fig. 8. TEM cross-sectional image of an AlCrMoNbZr/(AlCrMoNbZr)N 50 nm multilayer coating after He irradiation with a fluence of 8×10^{16} ion/cm²: (a) bright field image, (b) dark field image, and (c) cross-sectional HRTEM image in the region that was 1000 nm underneath the coating surface.

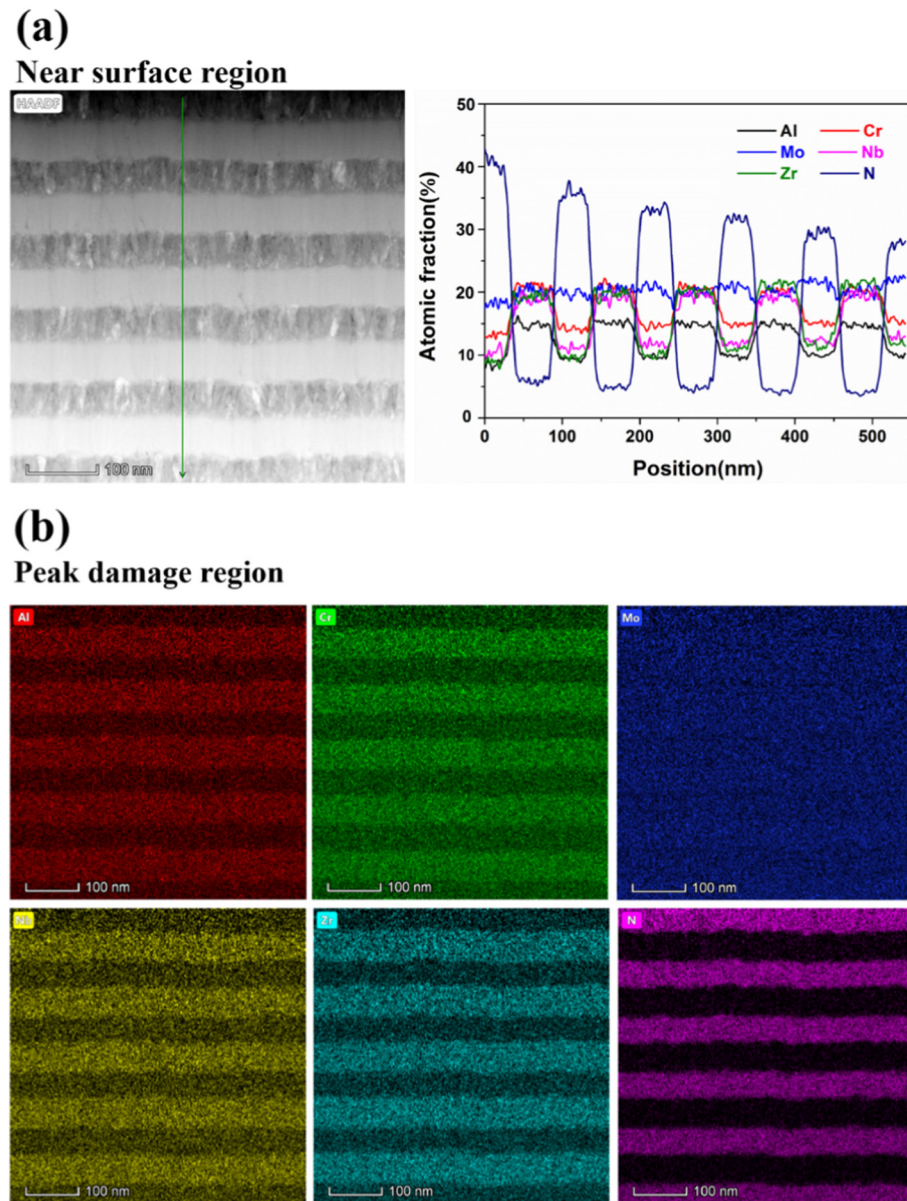


Fig. 9. EDS line scan and EDS mapping of AlCrMoNbZr/(AlCrMoNbZr)N 50 nm multilayer coating after He irradiation with a fluence of 8×10^{16} ion/cm²: (a) EDS line scan in the near surface region; (b) EDS mapping in the peak damage region.

The AlCrMoNbZr/(AlCrMoNbZr)N 50 nm multilayer coating He ion irradiated with a fluence of 8×10^{16} ion/cm² was also studied by TEM. Fig. 8 illustrates the cross-section TEM images of the implanted

AlCrMoNbZr/(AlCrMoNbZr)N 50 nm multilayer interface structures in different irradiated regions. No bubbles are observed in the bright-field and dark-field images of the AlCrMoNbZr/(AlCrMoNbZr)N 50 nm

multilayer coatings in the different irradiation regions, similarly to the TEM results of the AlCrMoNbZr/(AlCrMoNbZr)N 5 nm multilayer coating. Meanwhile, the coating has a clear layered structure in both the near-surface regions and peak damage regions. An EDS line scan of near-surface regions and EDS mapping of peak damage regions were performed to characterize the chemical composition of the AlCrMoNbZr/(AlCrMoNbZr)N 50 nm multilayer coating after irradiation, as shown in Fig. 9. The EDS line scan data of the near-surface regions show that the six elements of Al, Cr, Mo, Nb, Zr and N exhibit periodic changes without interdiffusion (Fig. 9(a)), and the EDS mapping data of the peak damage regions show that the five elements of Al, Cr, Nb, Zr and N have obvious layered distributions (Fig. 9(b)). Moreover, the microstructure of the irradiated multilayer coating was also investigated by high-resolution TEM, as shown in Fig. 8(c). It can be clearly seen that the multilayer coating has a distinct interface, in which the AlCrMoNbZr layer is amorphous and the (AlCrMoNbZr)N layer has an FCC structure. Meanwhile, the (AlCrMoNbZr)N layer contains a large number of columnar and amorphous regions. The amorphous regions across the (AlCrMoNbZr)N layer blocks the columnar crystals.

The results of the above multilayer coatings of AlCrMoNbZr/(AlCrMoNbZr)N 5 nm and 50 nm after He irradiation with a fluence of 8×10^{16} ion/cm² indicate that the combination of excellent irradiation resistance of the high-entropy alloy and the design of multilayer interface structure can effectively inhibit the growth of helium bubbles. Moreover, as the single layer thickness increased, the stability of the multilayer interface improved, which is beneficial for inhibiting the material swelling and further maintaining the critical service performance, such as the mechanical and corrosion performance required by the material in the light water reactor.

3.3. Mechanical properties and corrosion properties of irradiated multilayer coatings

The hardness of the as-deposited and He ion-irradiated AlCrMoNbZr/(AlCrMoNbZr)N multilayer coatings with different fluences are compared in Fig. 10(a). The hardness of the as-deposited AlCrMoNbZr/(AlCrMoNbZr)N 5 nm, 10 nm and 50 nm multilayer coatings was 17.1 GPa, 14.6 GPa and 15.8 GPa, respectively. However, the hardness of all multilayer coatings is lower than that of the deposited coating after He irradiation with fluences of 8×10^{15} and 8×10^{16} ion/cm². The change in coating hardness after irradiation is closely related to the thermal effect [28] and the introduction of He into coatings by irradiation [44]. The thermal effect is easily caused by beam heating during the irradiation process, which may cause the release of residual stress in the coating, thus leading to a decrease in the hardness of the coating. Conversely, the introduction of helium into the coating by irradiation can result in an increase in the hardness of the coating [44]. To investigate the effect of thermal effects on coating

hardness, the as-deposited AlCrMoNbZr/(AlCrMoNbZr)N 5 nm multilayer coating was annealed at the same time (4.5 h and 45 h, respectively) and temperature (300 °C) as the irradiated material. As shown in Fig. 10(b), the hardness of the coating after annealing is significantly lower than that of the as-deposited coating, consistent with that of the irradiated coating with a low fluence (8×10^{15} ion/cm²). Generally, low-temperature annealing tends to relax the residual stresses in coatings, leading to a decrease in the coating hardness. It can be concluded that the decrease in hardness of the AlCrMoNbZr/(AlCrMoNbZr)N multilayer coating is mainly caused by the thermal effect during irradiation. In addition, the hardness of coatings after irradiation with a high fluence is higher than that of irradiation with a lower fluence (Fig. 10(b)), due to the increase of helium concentration under irradiation with a higher fluence.

In addition, the influence of He ions on the corrosion resistance of all AlCrMoNbZr/(AlCrMoNbZr)N multilayer coatings was investigated by electrochemical testing. Polarization curves of irradiated AlCrMoNbZr/(AlCrMoNbZr)N 5 nm, 10 nm and 50 nm multilayer coatings were collected in 3.5% NaCl solution at room temperature (25 °C), as shown in Fig. 11(a), (b) and (c). The corresponding corrosion current density (i_{corr}) data are shown in Fig. 11(d). The anodic polarization curves of all samples are relatively flat and even horizontal compared to those of the unirradiated samples, implying that the multilayer coatings are more protective after He⁺ irradiation. As Fig. 11(d) depicts, the multilayer coating irradiated at 400 keV with a He⁺ fluence of 8×10^{15} ion/cm² has a lower i_{corr} compared to the unirradiated coating. With the fluence increasing to 8×10^{16} ion/cm², the i_{corr} of AlCrMoNbZr/(AlCrMoNbZr)N 10 nm and 50 nm multilayer coatings further decreased. Especially for the AlCrMoNbZr/(AlCrMoNbZr)N 50 nm multilayer coatings, the i_{corr} (0.58×10^{-8} A/cm²) decreases by approximately two orders of magnitude compared to the unirradiated coating (0.21×10^{-6} A/cm²). The reason is that the amorphous structure induced by irradiation traversed the columnar crystal, which can prevent the chloride ions from penetrating through the coating and thus enhanced the chloride ion corrosion resistance. In addition, the multilayer interfaces were entire and complete after irradiation, as shown in Fig. 8. A stable interface is beneficial for maintaining the corrosion resistance of the coating. However, the i_{corr} (6.6×10^{-8} A/cm²) of the AlCrMoNbZr/(AlCrMoNbZr)N 5 nm multilayer coating was improved after irradiation at 400 keV with a He⁺ fluence of 8×10^{16} ion/cm² compared to the unirradiated coating (5.8×10^{-8} A/cm²). Combined with the TEM results under He⁺ irradiation with high fluence, the interfacial mixing in the peak damage region could provide a channel for the penetration of chlorine ions, resulting in a decrease in the corrosion resistance of the coating against chloride ions.

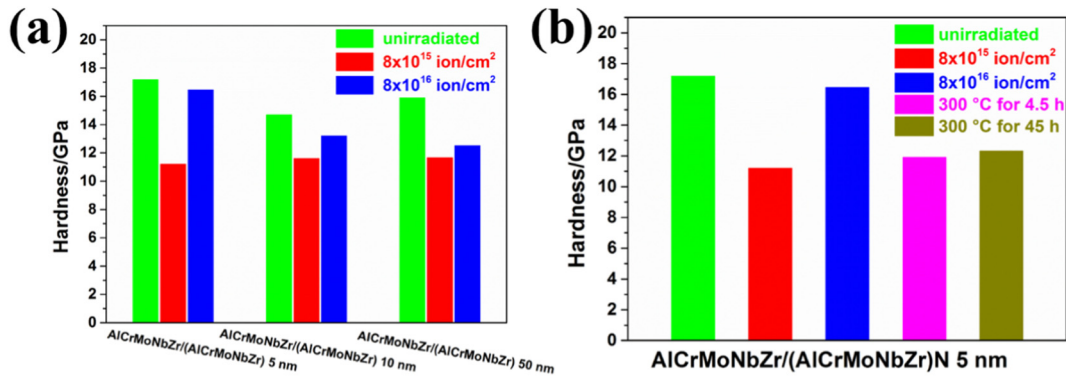


Fig. 10. (a) Comparison of hardness for as-deposited and ion irradiated AlCrMoNbZr/(AlCrMoNbZr)N with difference fluence; (b) hardness of AlCrMoNbZr/(AlCrMoNbZr)N 5 nm multilayer coating was annealed at the same time (4.5 h and 45 h, respectively) and temperature (300 °C) as the irradiated material.

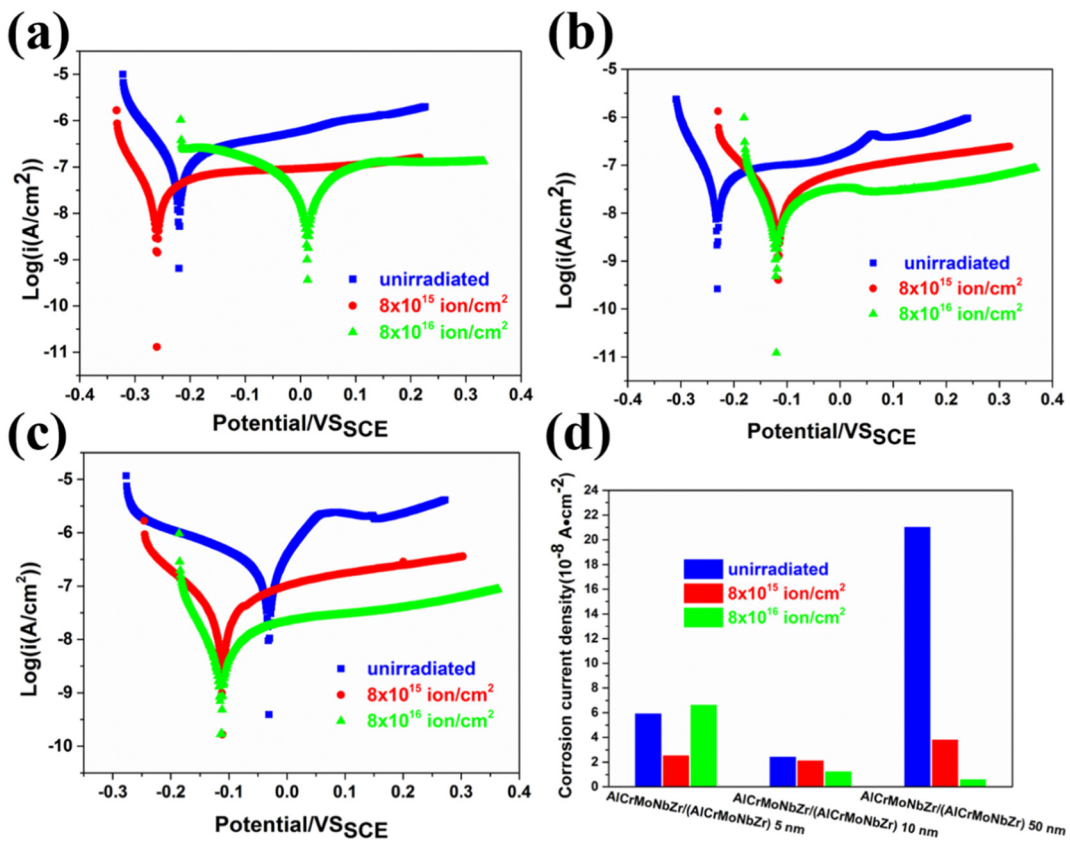


Fig. 11. Corrosion resistance of AlCrMoNbZr/(AlCrMoNbZr)N multilayer coating in 3.5% NaCl solution: (a) polarization curve of AlCrMoNbZr/(AlCrMoNbZr)N 5 nm multilayer coating; (b) polarization curve of AlCrMoNbZr/(AlCrMoNbZr)N 10 nm multilayer coating; (c) polarization curve of AlCrMoNbZr/(AlCrMoNbZr)N 50 nm multilayer coating; (d) corrosion current density of as-deposited and irradiated AlCrMoNbZr/(AlCrMoNbZr)N multilayer coating.

4. Conclusions

The interface structure, mechanical properties and electrochemical corrosion properties of AlCrMoNbZr/(AlCrMoNbZr)N multilayer coatings with equal individual layer thicknesses varies from 5 to 50 nm were investigated after subjected to He irradiation with different fluences. All multilayer coatings exhibited stable FCC structures, and no helium bubbles were observed in multilayer coatings after helium irradiation. He ion irradiation induced intermixing and chemical reactivity in the AlCrMoNbZr/(AlCrMoNbZr)N 5 nm multilayer coating at a high fluence, while the multilayer interfaces in the AlCrMoNbZr/(AlCrMoNbZr)N 50 nm multilayer coating were sharp, the elements did not interdiffuse and showed a layered distribution. The thermal effect caused by irradiation was the main factor that decreased the hardness of the coating to lower than that of the as-deposited coating, whereas the coating hardness recovered after He irradiation with a high fluence of irradiation hardening. In addition, the corrosion resistance of the irradiated multilayer coating was closely related to the integrity of the multilayer interface. The AlCrMoNbZr/(AlCrMoNbZr)N 50 nm multilayer coating with a complete interface had a lower corrosion current density than the AlCrMoNbZr/(AlCrMoNbZr)N 5 nm multilayer coating with intermixing, which was two orders of magnitude lower than the as-deposited coating. This study suggests that a high-entropy alloy multilayer coating with a thicker single layer exhibits better interface stability, mechanical properties and corrosion resistance.

Acknowledgements

This work is funded by the International Science and Technology Cooperation Programme of China (Grant No. 2015DFR60370), the National Natural Science Foundation of China (Grant No. 11475119)

and the Opening Project of Science and Technology on Reactor Fuel and Materials Laboratory (Grant No. STRFML-2018-19). Additionally, support by the Opening Project of Material Corrosion and Protection Key Laboratory of Sichuan Province (2015CL04) is gratefully acknowledged. The authors thank Dr. Zhang from ZKKF (Beijing) Science & Technology Co., Ltd. for the TEM measurements and the Ion Beam Center (IBC) at HZDR for performing the helium ion irradiation.

References

- [1] S.J. Zinkle, K.A. Terrani, J.C. Gehin, L.J. Ott, L.L. Snead, Accident tolerant fuels for LWRs: a perspective, *J. Nucl. Mater.* 448 (2014) 374–379.
- [2] B.R. Maier, B.L. Garcia-Diaz, B. Hauch, L.C. Olson, R.L. Sindelar, K. Sridharan, Cold spray deposition of Ti₂AlC coatings for improved nuclear fuel cladding, *J. Nucl. Mater.* 466 (2015) 1–6.
- [3] D.A. Roberts, K.E. Sickafus, Magnetron Sputtering and Corrosion of Ti-Al-C and Cr-Al-C Coatings for Zr-Alloy Nuclear Fuel Cladding, University of Tennessee, 2016 (M.S. thesis).
- [4] J.H. Park, H.G. Kim, J.Y. Park, Y.-I.I. Jung, D.J. Park, Y.H. Koo, High temperature steam-oxidation behavior of arc ion plated Cr coatings for accident tolerant fuel claddings, *Surf. Coat. Technol.* 280 (2015) 256–259.
- [5] B. Cheng, P. Chou, Y.J. Kim, Evaluations of Mo-alloy for light water reactor fuel cladding to enhance accident tolerance, *EPJ Nuclear Sci. Technol.* 2 (2016) 1–5.
- [6] E. Alat, A.T. Motta, R.J. Comstock, J.M. Partezana, D.E. Wolfe, Multilayer (TiN, TiAlN) ceramic coatings for nuclear fuel cladding, *J. Nucl. Mater.* 478 (2016) 236–244.
- [7] S.V. Ivanova, E.M. Glagovsky, K.Y. Nikonorov, I.I. Belugin, I.A. Khazov, Methods to increase corrosion stability and wear resistance of LWR active core zirconium components during operation and in conditions of loss-of-coolant accident, *Proceeding of LWR Fuel Performance Meeting/Top Fuel*, Charlotte, USA, 2013, pp. 334–350.
- [8] W. Zhang, R. Tang, Z.B. Yang, C.H. Liu, H. Chang, J.J. Yang, J.L. Liao, Y.Y. Yang, N. Liu, Preparation, structure, and properties of high-entropy alloy multilayer coatings for nuclear fuel cladding: a case study of AlCrMoNbZr/(AlCrMoNbZr)N, *J. Nucl. Mater.* 512 (2018) 15–24.
- [9] W. Zhang, R. Tang, Z.B. Yang, C.H. Liu, H. Chang, J.J. Yang, J.L. Liao, Y.Y. Yang, N. Liu, Preparation, structure, and properties of an AlCrMoNbZr high-entropy alloy

- coating for accident-tolerant fuel cladding, *Surface & Coatings Technology* 347 (2018) 13–19.
- [10] J.W. Yeh, S.K. Chen, S.J. Lin, J.Y. Gan, T.S. Chin, T.T. Shun, C.H. Tsau, S.Y. Chang, Nanostructured high-entropy alloys with multiple principal elements: novel alloy design concepts and outcomes, *Adv. Eng. Mater.* 6 (2004) 299–303.
- [11] V. Shivam, J. Basu, Y. Shadangi, M.K. Singh, N.K. Mukhopadhyay, Mechano-chemical synthesis, thermal stability and phase evolution in AlCoCrFeNiMn high entropy alloy, *J. Alloys Compd.* 757 (2018) 87–97.
- [12] J. Chen, X.Y. Zhou, W.L. Wang, B. Liu, Y.K. Lv, W. Yang, D. Xu, Y. Liu, A review on fundamental of high entropy alloys with promising high-temperature properties, *J. Alloys Compd.* 760 (2018) 15–30.
- [13] O.N. Senkov, S.V. Senkova, C. Woodward, Effect of aluminum on the microstructure and properties of two refractory high-entropy alloys, *Acta Mater.* 68 (2014) 214–228.
- [14] Y. Zou, J.M. Wheeler, H. Ma, P. Okle, R. Spolenak, Nanocrystalline high-entropy alloys: a new paradigm in high-temperature strength and stability, *Nano Lett.* 17 (2017) 1569–1574.
- [15] Y.X. Liu, C.Q. Cheng, J.L. Shang, R. Wang, P. Li, J. Zhao, Oxidation behavior of high-entropy alloys Al_xCoCrFeNi ($x = 0.15, 0.4$) in supercritical water and comparison with HR3C steel, *Trans. Nonferr. Met. Soc. China* 25 (2015) 1341–1351.
- [16] S.Q. Xia, X. Yang, T.F. Yang, S. Liu, Y. Zhang, Irradiation resistance in AlxCrCoFeNi high entropy alloys, *The Minerals, Metals and Materials Society* 67 (2015) 2340–2344.
- [17] C.Y. Lu, L.L. Niu, N.J. Chen, K. Jin, T. Yang, P.Y. Xiu, Y.W. Zhang, F. Gao, H.B. Bei, S. Shi, M.R. He, I.M. Robertson, W.J. Weber, L.M. Wang, Enhancing radiation tolerance by controlling defect mobility and migration pathways in multicomponent single-phase alloys, *Nat. Commun.* 7 (2016) 13564–13572.
- [18] F.F. Komarova, A.D. Pogrebnyak, S.V. Konstantinov, Radiation resistance of high-entropy nanostructured (Ti, Hf, Zr, V, Nb) N coatings, *Phys. Nanostruct.* 60 (2015) 1519–1524.
- [19] T. Nagase, P.D. Rack, J.H. Noh, T. Egami, In-situ TEM observation of structural changes in nano-crystalline CoCrCuFeNi multicomponent high-entropy alloy (HEA) under fast electron irradiation by high voltage electron microscopy (HVEM), *Intermetallics* 59 (2015) 32–42.
- [20] A.D. Pogrebnyak, O.V. Bondar, S.O. Borba, G. Abadias, P. Konarski, S.V. Plotnikov, V.M. Beresnev, L.G. Kassanova, P. Drodziel, Nanostructured multielement (TiHfZrNbVTa)N coatings before and after implantation of N⁺ ions (10^{18} cm^2): their structure and mechanical properties, *Nucl. Inst. Methods Phys. Res. B* 385 (2016) 74–83.
- [21] J. Wang, S.H. Liu, D.L. Ren, T. Shao, P. Eklund, R. Huang, Y.B. Zhu, F. Huang, S.Y. Du, Z.G. Wang, J.M. Xue, Y.G. Wang, Q. Huang, Microstructural evolution of epitaxial Ti₃AlC₂ film on sapphire under ion irradiation and nanoindentation-induced deformation, *J. Nucl. Mater.* 509 (2018) 181–187.
- [22] E. Aydogan, J.S. Weaver, S.A. Maloy, O. El-Atwani, Y.Q. Wang, N.A. Mara, Microstructure and mechanical properties of FeCrAl alloys under heavy ion irradiations, *J. Nucl. Mater.* 503 (2018) 250–262.
- [23] A. Wu, J. Ribis, J.-C. Brachet, E. Clouet, F. Leprétre, E. Bordas, B. Arnal, HRTEM and chemical study of an ion-irradiated chromium/zircaloy-4 interface, *J. Nucl. Mater.* 504 (2018) 289–299.
- [24] X.M. Bai, A.F. Voter, R.G. Hoagland, M. Nastasi, B.P. Uberuaga, Efficient annealing of radiation damage near grain boundaries via interstitial emission, *Science* 327 (2010) 1631–1634.
- [25] M.J. Demkowicz, A. Misra, A. Caro, The role of interface structure in controlling high helium concentrations, *Curr. Opin. Solid State Mater. Sci.* 16 (2012) 101–108.
- [26] A. Misra, M. Demkowicz, X. Zhang, R.G. Hoagland, The radiation damage tolerance of ultra-high strength nanolayered composites, *JOM* 59 (2007) 62–65.
- [27] X. Zhang, Nan Li, O. Anderoglu, H. Wang, J.G. Swadener, T. Höchbauer, A. Misra, R.G. Hoagland, Nanostructured Cu/Nb multilayers subjected to helium ion-irradiation, *Nucl. Inst. Methods Phys. Res. B* 261 (2007) 1129–1132.
- [28] M. Callisti, M. Karlik, T. Polcar, Bubbles formation in helium ion irradiated Cu/W multilayer nanocomposites: effects on structure and mechanical properties, *J. Nucl. Mater.* 473 (2016) 18–27.
- [29] E.G. Fu, J. Carter, G. Swadener, A. Misra, L. Shao, H. Wang, X. Zhang, Size dependent enhancement of helium ion irradiation tolerance in sputtered Cu/V nanolaminates, *J. Nucl. Mater.* 385 (2009) 629–632.
- [30] Nan Li, E.G. Fu, H. Wang, J.J. Carter, L. Shao, S.A. Maloy, A. Misra, X. Zhang, He ion irradiation damage in Fe/W nanolayer films, *J. Nucl. Mater.* 389 (2009) 233–238.
- [31] Nan Li, M. S. Martin, O. Anderoglu, A. Misra, L. Shao, H. Wang, X. Zhang, He ion irradiation damage in Al/Nb multilayer, *J. Appl. Phys.*, 105(2009) 123522–123530.
- [32] H.X. Zhang, F. Ren, Y.Q. Wang, M.Q. Hong, X.H. Xiao, W.J. Qin, C.Z. Jiang, In situ TEM observation of helium bubble evolution in V/Ag multilayer during annealing, *J. Nucl. Mater.* 467 (2015) 537–543.
- [33] I. Kim, L. Jiao, F. Khatkhatay, M.S. Martin, J. Lee, L. Shao, X. Zhang, J.G. Swadener, Y.Q. Wang, J. Gan, J.I. Cole, H. Wang, Size-dependent radiation tolerance in ion irradiated TiN/AlN nanolayer films, *J. Nucl. Mater.* 441 (2013) 47–53.
- [34] L. Jiao, A. Chen, M.T. Myers, M.J. General, L. Shao, X. Zhang, H. Wang, Enhanced ion irradiation tolerance properties in TiN/MgO nanolayer film, *J. Nucl. Mater.* 434 (2013) 217–222.
- [35] F.F. Zhang, X. Wang, J.B. Wierschke, L.M. Wang, Helium bubble evolution in ion irradiated Al/B₄C metal matrix composite, *Scr. Mater.* 109 (2015) 28–33.
- [36] Y. Xu, J.A. Aguiar, S.K. Yadav, O. Anderoglu, J.K. Baldwin, Y.Q. Wang, J.A. Valdez, A. Misra, H.M. Luo, B.P. Uberuaga, N. Li, Solute redistribution and phase stability at FeCr/TiO_{2-x} interfaces under ion irradiation, *Acta Mater.* 89 (2015) 364–373.
- [37] S.J. Zinkle, G.S. Was, Materials challenges in nuclear energy, *Acta Mater.* 61 (2013) 735–758.
- [38] N. Available, Characterizing Neutron Exposures in Ferritic Steels in Terms of Displacements per Atom (DPA), Annu. Book ASTM Stand, (1981), pp. 1211–1217 (United States. Medium: X; Size).
- [39] S. Guo, Q. Hu, C. Ng, C.T. Liu, More than entropy in high-entropy alloys: forming solid solutions or amorphous phase, *Intermetallics* 41 (2013) 96–103.
- [40] A. Inoue, High strength bulk amorphous alloys with low critical cooling rates, *Materials Transactions Jim* 36 (1995) 866–875.
- [41] I. Petrov, L. Hultman, L.E. Sundgren, J.E. Greene, Polycrystalline TiN films deposited by reactive bias magnetron sputtering: effects of ion bombardment on re-sputtering rates, film composition, and microstructure, *J. Vac. Sci. Technol. A* 10 (1992) 265–272.
- [42] W. Ensinger, Growth of thin films with preferential crystallographic orientation by ion bombardment during deposition, *Surf. Coat. Technol.* 65 (1994) 90–105.
- [43] L. Hultman, J.E. Sundgren, J.E. Greene, D.B. Bergstrom, I. Petrov, High-flux low-energy ($\approx 20 \text{ eV}$) N₂⁺ ion irradiation during TiN deposition by reactive magnetron sputtering: effects on microstructure and preferred orientation, *J. Appl. Phys.* 78 (1995) 5395–5403.
- [44] F.H. Kong, M. Qu, S. Yan, A.L. Zhang, S.X. Peng, J.M. Xue, Y.G. Wang, Helium-induced hardening effect in polycrystalline tungsten, *Nucl. Inst. Methods Phys. Res. B* 406 (2017) 643–647.
- [45] D.C. Tsai, M.J. Deng, Z.C. Chang, B.H. Kuo, E.C. Chen, S.Y. Chang, F.S. Shieh, Oxidation resistance and characterization of (AlCrMoTaTi)-Six-N coating deposited via magnetron sputtering, *J. Alloys Compd.* 647 (2015) 179–188.
- [46] P. Sigmund, A. Gras-Martí, Theoretical aspects of atomic mixing by ion beams, *Nucl. Inst. Methods* 182 (1981) 25–41.
- [47] W.L. Johnson, Y.T. Cheng, M. Van Rossum, M.-A. Nicolet, When is thermodynamics relevant to ion-induced atomic rearrangements in metals? *Nucl. Inst. Methods Phys. Res. B* 7 (1985) 657–665.
- [48] G.H. Vineyard, Thermal spikes and activated processes, *Radiat. Eff.* 29 (1976) 245–248.